Athermal silicon ring resonators clad with titanium dioxide for 1.3μm wavelength operation

Shaoqi Feng,[1] Kuanping Shang,[1] Jock T. Bovington,[2] Rui Wu,[2] Binbin Guan,[1] Kwang-Ting Cheng,[2] John E. Bowers,[2] and S. J. Ben Yoo[1,*]

[1]Department of Electrical and Computer Engineering, University of California, Davis, CA 95616, USA
[2]Department of Electrical and Computer Engineering, University of California, Santa Barbara, CA 93106, USA
[*]sbyoo@ucdavis.edu

Abstract: We investigate the athermal characteristics of silicon waveguides clad with TiO_2 designed for 1.3 µm wavelength operation. Using CMOS-compatible fabrication processes, we realize and experimentally demonstrate silicon photonic ring resonators with resonant wavelengths that vary by less than 6 pm/°C at 1.3 µm. The measured ring resonance wavelengths across the 20-50°C temperature range show nearly complete cancellation of the first-order thermo-optical effects and exhibit second-order thermo-optical effects expected from the combination of TiO_2 and Si.

References and links

1. W. Bogaerts, P. De Heyn, T. Van Vaerenbergh, K. De Vos, S. Kumar Selvaraja, T. Claes, P. Dumon, P. Bienstman, D. Van Thourhout, and R. Baets, "Silicon microring resonators," Laser Photonics Rev. **6**(1), 47–73 (2012).
2. S. Feng, T. Lei, H. Chen, H. Cai, X. Luo, and A. W. Poon, "Silicon photonics: from a microresonator perspective," Laser Photonics Rev. **6**(2), 145–177 (2012).
3. K. Padmaraju, D. F. Logan, X. Zhu, J. J. Ackert, A. P. Knights, and K. Bergman, "Integrated thermal stabilization of a microring modulator," Opt. Express **21**(12), 14342–14350 (2013).
4. W. A. Zortman, A. L. Lentine, D. C. Trotter, and M. R. Watts, "Bit-error-rate monitoring for active wavelength control of resonant modulators," IEEE Micro **33**(1), 42–52 (2013).
5. Y. Zhang, Y. Li, S. Feng, and A. W. Poon, "Towards adaptively tuned silicon microring resonators for optical networks-on-chip applications," IEEE J. Sel. Top. Quantum Electron. **20**(4), 136–149 (2014).
6. B. Guha, B. B. C. Kyotoku, and M. Lipson, "CMOS-compatible athermal silicon microring resonators," Opt. Express **18**(4), 3487–3493 (2010).
7. B. Guha, K. Preston, and M. Lipson, "Athermal silicon microring electro-optic modulator," Opt. Lett. **37**(12), 2253–2255 (2012).
8. L. Zhou, K. Okamoto, and S. J. B. Yoo, "Athermalizing and trimming of slotted silicon microring resonators with UV-sensitive PMMA upper-cladding," IEEE Photonics Technol. Lett. **21**(17), 1175–1177 (2009).
9. J. Teng, P. Dumon, W. Bogaerts, H. Zhang, X. Jian, X. Han, M. Zhao, G. Morthier, and R. Baets, "Athermal Silicon-on-insulator ring resonators by overlaying a polymer cladding on narrowed waveguides," Opt. Express **17**(17), 14627–14633 (2009).
10. V. Raghunathan, W. N. Ye, J. Hu, T. Izuhara, J. Michel, and L. Kimerling, "Athermal operation of silicon waveguides: spectral, second order and footprint dependencies," Opt. Express **18**(17), 17631–17639 (2010).
11. S. S. Djordjevic, K. Shang, B. Guan, S. T. S. Cheung, L. Liao, J. Basak, H.-F. Liu, and S. J. B. Yoo, "CMOS-compatible, athermal silicon ring modulators clad with titanium dioxide," Opt. Express **21**(12), 13958–13968 (2013).
12. K. Shang, S. S. Djordjevic, J. Li, L. Liao, J. Basak, H.-F. Liu, and S. J. B. Yoo, "CMOS-compatible titanium dioxide deposition for athermalization of silicon photonic waveguides," in *Conference on Lasers and Electro-Optics (CLEO)* (Optical Society of America, 2013), p. CF2I.5.
13. B. Guha, J. Cardenas, and M. Lipson, "Athermal silicon microring resonators with titanium oxide cladding," Opt. Express **21**(22), 26557–26563 (2013).
14. J. Bovington, R. Wu, K.-T. Cheng, and J. E. Bowers, "Thermal stress implications in athermal TiO2 waveguides on a silicon substrate," Opt. Express **22**(1), 661–666 (2014).
15. V. Trepakov, A. Dejneka, P. Markovin, A. Lynnyk, and L. Jastrabik, "A "soft electronic band" and the negative thermooptic effect in strontium titanate," New J. Phys. **11**(8), 083024 (2009).
16. H.-H. Chang, A. W. Fang, M. N. Sysak, H. Park, R. Jones, O. Cohen, O. Raday, M. J. Paniccia, and J. E. Bowers, "1310nm silicon evanescent laser," Opt. Express **15**(18), 11466–11471 (2007).

17. B. J. Frey, D. B. Leviton, and T. J. Madison, "Temperature-dependent refractive index of silicon and germanium," Proc. SPIE **6273**, 62732J (2006).

1. Introduction

Photonic integration brings various functionalities from multiple chips into a single chip while greatly reducing the number of optical interfaces, optical packages, and thermo-electric coolers (TECs) associated with the multiple discrete chips. Among many photonic integration platforms including GaAs, InP, silica, and other material platforms, silicon photonics has rapidly emerged as a viable and attractive integration platform [1,2] due to the availability of high-quality oxides that enable low-loss and compact waveguides while exploiting widely available CMOS fabrication facilities. However, practical deployment of silicon photonics exploiting multi-wavelength parallelism is seriously suffering from its strong temperature dependent characteristics. Silicon has a relatively large thermo-optical coefficient (TOC) of 1.84×10^{-4}/°C, which is more than an order of magnitude greater than that of silica. As a result, typical silicon photonic devices suffer from ~0.1 nm/°C wavelength dependence with temperature variations, and they require optical packages with TECs for practical deployment. Since athermal silica photonic integrated circuits are already widely deployed in communication networks in simple packages without TECs, the cost advantages and reliability of silicon photonics suffer from their strong temperature dependence.

There has been in large, three main methods to overcome this challenge. The first method has been to introduce integrated heaters onto the silicon photonic devices to actively monitor and control the temperature using feedback control circuits, but this adds complexity and additional power consumption [3–5]. The second method has been to integrate a ring resonator with a Mach-Zehnder interferometer which compensates the thermal dependence of the ring [6,7], but this solution increases the total footprint and typically shows significant wavelength dependence. The third method has been to introduce an upper cladding made of a material with negative TOC to compensate for the positive TOC of silicon. Early demonstrations have utilized polymers with negative TOC as an uppercladding to realize athermal silicon photonics [8–10]. Recently, CMOS-compatible fabrication process involving titanium dioxide (TiO$_2$) has been demonstrated and investigated [11–14] for operation in the 1.550 nm wavelength range. TiO$_2$ has a relatively strong negative TOC of approximately - 1 $\times$ 10^{-4}/°C ~- 2 $\times$ 10^{-4}/°C around 1550 nm due to presence of a soft electronic band [15] and is already adopted in CMOS processes due to superior reliability. On the other hand, athermal operation of silicon photonic devices in the 1310 nm wavelength range is very important because semiconductor lasers have higher T_0 values and optical fibers have lower dispersion at this range compared with the 1550 nm wavelength range [16]. In this paper, we investigate athermal operation of silicon ring resonators overclad with TiO$_2$ cladding in the 1310 nm wavelength range. The CMOS compatible fabrication led to TiO$_2$-clad silicon ring resonators that showed near complete cancelation of the first order thermo-optical dependence and exhibited residual second order thermo-optical effects in the 1310 nm wavelength range.

2. Design of athermal Si-TiO$_2$ waveguides

An athermal silicon photonic waveguide consists of silicon core, buried oxide (BOX) undercladding and TiO$_2$ overcladding. Figure 1(a) shows the schematic cross-section of the athermal waveguide. The equivalent thermo-optic coefficient ($\frac{dn_{eff}}{dT}$) of the TiO$_2$-overclad silicon waveguide (Si-TiO$_2$) can be expressed as

$$\frac{dn_{eff}}{dT} = \sum_k \frac{d(\Gamma_k n_k)}{dT} = \sum_k \left[n_k \frac{d(\Gamma_k)}{dT} + \Gamma_k \frac{d(n_k)}{dT} \right] \approx \sum_k \Gamma_k \frac{dn_k}{dT} = \Gamma_{Si} \frac{dn_{Si}}{dT} + \Gamma_{SiO_2} \frac{dn_{SiO_2}}{dT} + \Gamma_{TiO_2} \frac{dn_{TiO_2}}{dT}$$

$$(1)$$

where n_{eff} is the effective index of the waveguide, Γ_k is the confinement factor of the k-th constituent part including the core, over-clad, and under-clad materials, T is the temperature, and $\dfrac{dn_k}{dT}$ is the thermo-optical coefficient of the k-th constituent material. The approximation in the Eq. (1) is valid to first order in $\dfrac{d}{dT}$ because Γ_k depends on $\dfrac{d(n_k)}{dT}$ indirectly. We will verify this assumption later in this paper. The athermal condition of a Si-TiO$_2$ waveguide requires $\dfrac{dn_{eff}}{dT}$ = 0. To first order, we can design the waveguide geometry to satisfy this athermal condition. In addition, the magnetron sputtering condition affects the density of the amorphous TiO$_2$ over-cladding, which also affects the result of the athermal condition. Figure 1(b) shows the calculated $\dfrac{dn_{eff}}{dT}$ at 1310 nm for three refractive index values of TiO$_2$ as a function of the waveguide core width. The TOC values of Si, SiO$_2$ and TiO$_2$ used in the simulation are 1.8×10^{-4}, 1×10^{-5} and -2×10^{-4} /°C, respectively [11]. For the measured TiO$_2$ refractive index of 2.4, the waveguide core width is chosen to be 220nm for athermal operation at 1310 nm wavelength.
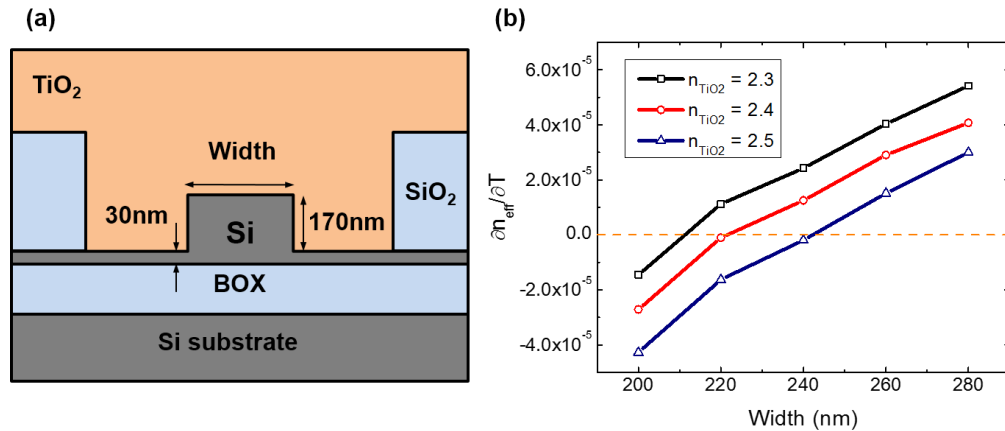

Fig. 1. (a) A cross-sectional schematic of athermal Si-TiO$_2$ waveguide. (b) Calculated dn_{eff}/dT as a function of the waveguide width for different refractive index values of TiO$_2$ cladding for 1310 nm operation.

3. Device fabrication

Figure 2 illustrates the fabrication process. The device fabrication utilized a 150mm silicon-on-insulator (SOI) wafer with 220nm thick top silicon and 3µm thick buried oxide layers. The top silicon layer is thinned down to 200nm by thermal oxidation. A silicon nitride hard mask of 30nm is deposited by low-pressure chemical vapor deposition (LPCVD). The ring resonator structures are patterned with 248nm projection lithography followed by reactive ion etching (RIE) with CF$_4$ for nitride and HBr for silicon. Then the ring waveguide structures are thermally oxidized with the hard mask still on top in order to smooth the sidewalls and to reduce the waveguide width below the lithography resolution of 250 nm dimension. The oxide and hard mask are then stripped in hydrogen fluoride and hot phosphoric acid, respectively. Figure 3 shows the scanning electronic microscopy (SEM) images of the fabricated device before TiO$_2$ cladding deposition. The ring resonator has a radius of 25 µm and a gap spacing of 550nm between ring and straight waveguides. The waveguide core has a width of 200nm and a slab thickness of 30nm. At the two end points of the coupling waveguides at the facet are inverse tapers with tip widths of 200nm to facilitate low-loss optical coupling.
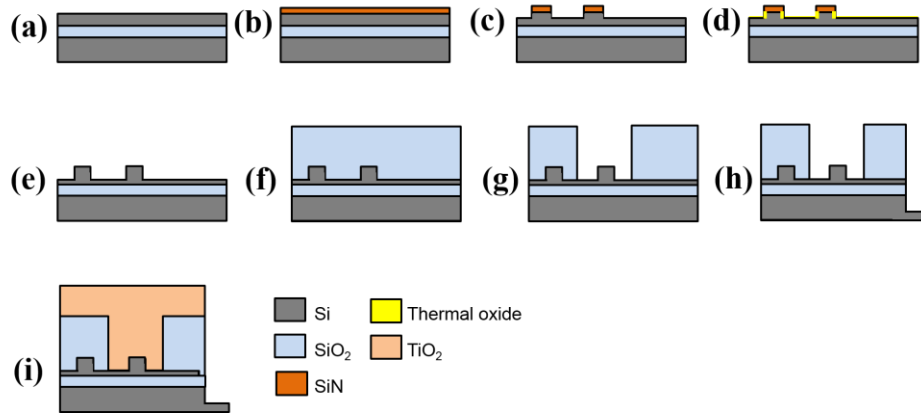
Fig. 2. Fabrication process steps: (a) Initial SOI wafer. (b) SiN hard mask deposition. (c) Waveguide layer patterning. (d) Thermal oxidation to reduce waveguide width. (e) SiN and thermal SiO_2 strip. (f) SiO_2 layer deposition. (g) Trench opening for TiO_2 cladding. (h) Deep etch for waveguide edge coupler. (i) TiO_2 cladding deposition.

The patterned devices are then deposited with 1μm thick SiO_2 by LPCVD. The trench for TiO_2 cladding is opened by CF_4 RIE etching followed by wet etching. The waveguide facet is deep reactive-ion etched (DRIE) by 100μm to accommodate fiber edge coupling. Finally TiO_2 cladding of 1.3 μm thickness is deposited by magnetron-sputtering for athermal operation. The relatively thick (1.3 μm) TiO_2 cladding was chosen to suppress optical scattering from the air-TiO_2 interface, and the optimal sputtering condition of 360W RF power and 12% oxygen content [11] was used to realize low loss TiO_2 cladding.
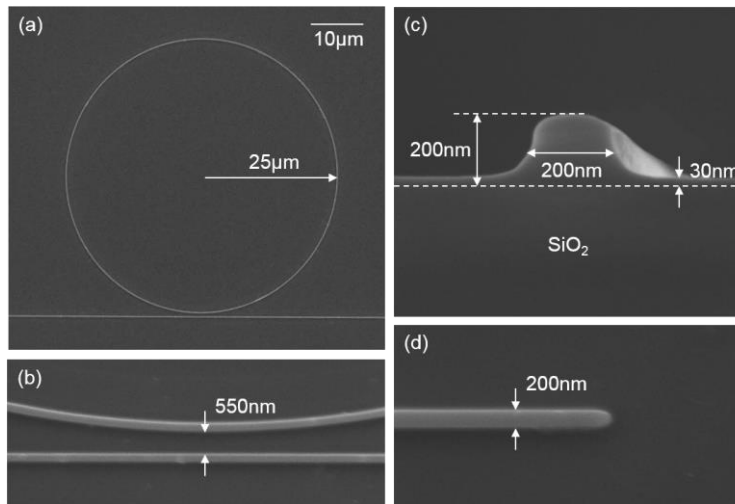

Fig. 3. Waveguide geometries. (a) Top-view SEM image of a ring resonator before TiO_2 cladding deposition; (b) Ring-to-bus waveguide coupling region; (c) Cross-sectional SEM image of a waveguide before TiO_2 cladding deposition; (d) Top-view SEM image of an inverse taper.

4. Device characterization

Transmission spectra measurements utilize a tunable laser and a photodiode with a device in the interferometer of the optical vector network analyzer (OVNA). The OVNA interferometer utilizes a pair of single-mode lensed fiber couplers with 2.5μm diameter spot sizes ($1/e^2$) to interface with the inverse tapers of the Si-TiO_2 waveguide at input and output facets to launch light into and to collect light from the athermal Si-TiO_2 ring resonator. The silicon photonic

chip containing the Si-TiO$_2$ ring resonators is mounted on a stage with a thermo-electric cooler (TEC) in order to control the device temperature with better than 0.1°C accuracy. We measured the transmission spectra of the Si-TiO$_2$ ring resonators as well as control devices (Si-SiO$_2$ ring resonators) overclad with SiO$_2$ instead of TiO$_2$ prepared on the same silicon photonic wafer. Figure 4 shows the measured transmission spectra of the two types of devices: Si-SiO$_2$ ring resonators and Si-TiO$_2$ ring resonators. The device with SiO$_2$ cladding shows a significant resonant wavelength redshift of 0.86 nm over 15°C variations. The resonance extinction ratio also changes when temperature increases, which may result from the temperature-induced change of coupling coefficient between ring and bus waveguides. The device with TiO$_2$ cladding shows less than 0.1 nm over the same temperature range, which is below the full width at the half maximum (FWHM) linewidth of 0.25 nm for the resonator. We extract the propagation losses of the waveguides by fitting the transmission spectra of the ring resonators. The propagation losses of 200nm waveguide core width with SiO$_2$ and TiO$_2$ cladding are 7 dB/cm and 20 dB/cm, respectively. Thus the extra loss for TiO$_2$ cladding as compared to SiO$_2$ cladding is 13 dB/cm, which is comparable to other existing results in 1550nm wavelength range [11,13].
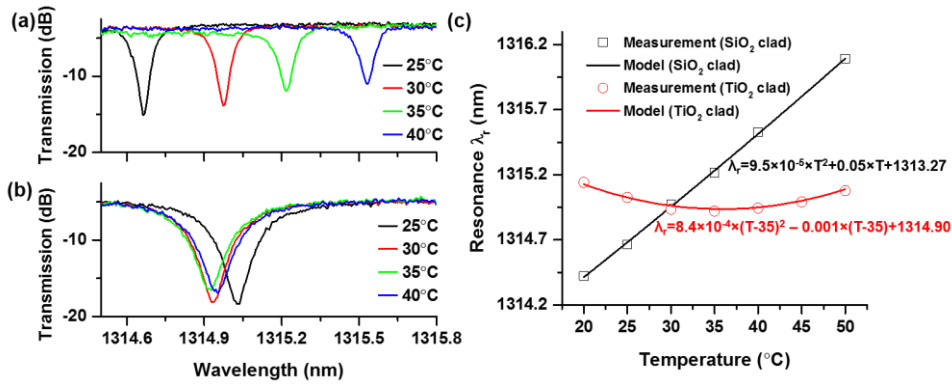

Fig. 4. (a) – (b) Measured transmission spectra at various temperature of the devices with (a) SiO$_2$ and (b) TiO$_2$ over cladding. (c) Resonance wavelength λ_r as a function of temperature for the devices of 200nm width with SiO$_2$ and TiO$_2$ cladding.

Figure 4(c) shows the measured resonance wavelength λ_r as a function of temperature for the devices of 200nm waveguide core width with SiO$_2$ and TiO$_2$ cladding. The curve-fit parameter to this measured data shows a wavelength shift of 50 pm/°C for the ring resonator with SiO$_2$ cladding. The curve-fit parameter to the data obtained for the ring resonator with TiO$_2$ cladding shows nearly complete cancellation to first order (< 6 pm/°C) while exhibiting the second order dependence at 0.8 pm/°C^2 centered at the design temperature of 35°C. The net result was less than 0.2 nm variation in the 20-50 °C temperature range.

In order to explain the quadratic dependency of wavelength upon temperature, second-order material TOCs as well as the confinement factor dependence on the first order material TOCs have to be taken into consideration. Material TOC can be expressed as:

$$dn/dT = \beta + \gamma \cdot T \tag{2}$$

where β is the first-order thermo-optical coefficient and γ is the second-order thermo-optical coefficient. The resonance wavelength λ_r of a ring resonator can be expressed as:

$$m\lambda_r = 2\pi n_{eff}(\lambda_r, T)R(T) \tag{3}$$

where m is the mode order. Hence its thermal dependency has the form:

$$\frac{d\lambda_r}{dT} = \frac{n_{eff}\lambda_r}{n_g R}\frac{dR}{dT} + \frac{\lambda_r}{n_g}\frac{dn_{eff}}{dT} \approx \frac{\lambda_r}{n_g}\left(n_{eff}\alpha_{sub} + \frac{dn_{eff}}{dT}\right) \qquad (4)$$

where n_g is the group index and α_{sub} is the thermal expansion coefficient of the silicon substrate which dominates the expansion of the path length. dn_{eff}/dT can be expressed as a linear superposition of TOCs of constituent materials:

$$\frac{dn_{eff}}{dT} = \sum_k \frac{d(\Gamma_k n_k)}{dT} = \sum_k\left[n_k\frac{d(\Gamma_k)}{dT} + \Gamma_k\frac{d(n_k)}{dT}\right] \approx \sum_k \Gamma_k \cdot dn_k/dT = \sum_k \Gamma_k \cdot (\beta_k + \gamma_k \cdot T)$$

$$(5)$$

Here, Γ_k is the confinement factor of each constituent part. Again, we assume that the $d\Gamma/dT$ induced second-order effect is negligible and proceed with the approximation in Eq. (5) similarly as in Eq. (1). Plug Eq. (4) into Eq. (3) and we can get $d\lambda_r/dT$ as a first-order polynomial function of temperature T which can explain the quadratic relationship between wavelength and temperature. The TOC of silicon at 1310 nm is reported as $1.834\times10^{-4} + 4.887\times10^{-7}\cdot T$ [17], where T is in unit of °C. The $\beta_{SiO_2} = 1\times10^{-5}$/°C and γ_{SiO_2} is assumed to be 0. The TOC of TiO$_2$ is calculated to be $-3.07\times10^{-4} + 4.45\times10^{-6}\cdot T$ based on fitting the measurement data.

Our simulation for the waveguide with a core width of 200nm and TiO$_2$ overcladding indicates that the $d\Gamma/dT$ induced second-order coefficient $d^2\lambda_r/dT^2 = 2.3\times10^{-5}\,\text{nm}/\,^oC^2$, which qualitatively agrees with the result in [10]. This second-order coefficient is much smaller than the one observed in our measurements (8×10^{-4}nm/°C^2), which verifies the approximation of neglecting $d\Gamma/dT$ in Eqs. (1) and (5).

The temperature-dependent wavelength shift can be varied at different spectral ranges. We measured the transmission spectra from 1270 nm to 1340 nm over the 20-50°C temperature range. Figures 5(a)-5(c) show the measured resonance wavelength shift as a function of temperature at various spectral ranges. We extracted the slope of temperature-dependent wavelength shift dλ$_r$/dT at T = 35°C. Figure 5(d) shows the dλ$_r$/dT as a function of wavelength. At 1270nm wavelength, resonance redshifts when temperate increases and dλ$_r$/dT is ~8pm/°C. At 1310nm wavelength, resonance wavelength first blueshifts and then redshifts as temperature rises, and dλ$_r$/dT at T = 35°C is close to zero. At 1340nm wavelength, resonance wavelength blueshifts as temperature rises and dλ$_r$/dT at T = 35°C is approximately −8pm/°C. For a fixed waveguide geometry, when the wavelength becomes longer, mode confinement increases in TiO$_2$ cladding, which contributes to the resonance blueshift and athermalization.
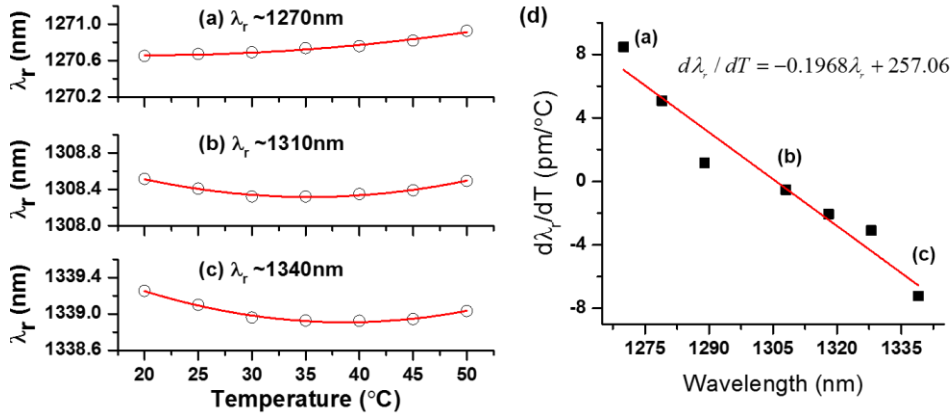
Fig. 5. (a) – (c) Measured (black circle) and quadratically fitted (red line) resonance wavelength shift as a function of temperature. The device with a waveguide width of 200nm is measured at various spectral ranges around (a) 1270nm, (b) 1310nm and (c) 1340nm. (d) Temperature-dependent wavelength shift $d\lambda_r/dT$ at T = 35°C as a function of wavelength. Black square: extracted $d\lambda_r/dT$ from the measurement result. Red line: linear fitted $d\lambda_r/dT$ at T = 35°C as a function of wavelength.

The temperature-dependent wavelength shift is also varied for different waveguide core widths. For a wavelength division multiplexing (WDM) application, the athermal operation of silicon ring resonators at different wavelengths can be achieved by appropriately designing the waveguide core width. Figure 6 shows the measured transmission spectra at various temperatures of the ring resonators with different core widths. The 200nm and 220nm wide devices achieve athermal operation at around 1315nm and 1336nm, respectively.
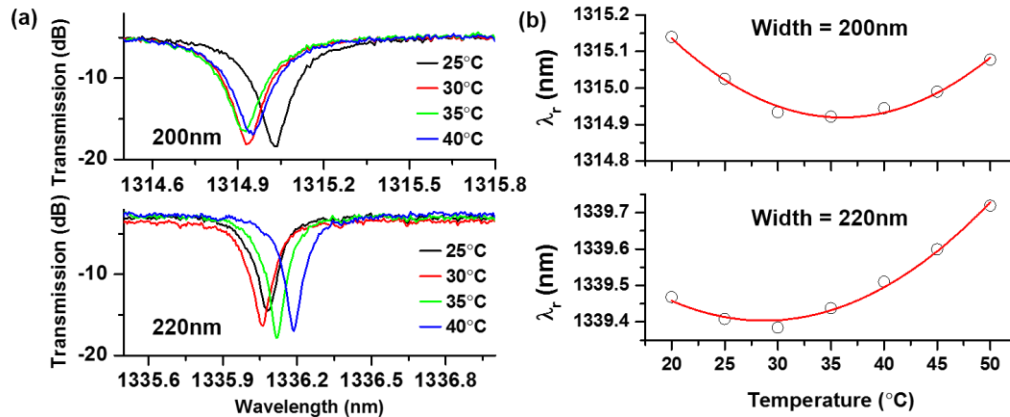

Fig. 6. (a) Measured transmission spectra at various temperature of the devices with 200nm and 220nm widths. (b) Measured resonance wavelength λ_r as a function of temperature for the devices with 200nm and 220nm widths.

5. Conclusions

We demonstrate an athermal silicon ring resonator clad with TiO_2 cladding and measure temperature-dependent resonant wavelength shifts less than 6 pm/°C, exhibiting second order effects near 1310 nm. In order to athermalize silicon photonic devices over a wide temperature range, the waveguide geometries, first and second order TOC values of the materials, and operating wavelengths have to be carefully considered. In particular, the second order effects of TOC of TiO_2 need to be included in the design and operation near the athermal condition.

Acknowledgment